

Volume diffusion modelling of a sheared granular gas

Duncan Dockar¹, M. H. Lakshminarayana Reddy², Matthew K. Borg¹, and S. Kokou Dadzie^{*2}

¹Institute for Multiscale Thermofluids, School of Engineering, University of Edinburgh,
Edinburgh EH9 3FB, UK

²School of Engineering and Physical Sciences, Heriot-Watt University, Edinburgh EH14 4AS,
Scotland, UK

March 5, 2024

Abstract

Continuum fluid dynamic models based on the Navier–Stokes–Fourier (NSF) equations have previously been used to simulate granular media undergoing fluid-like shearing. These models, however, typically fail to predict the flow behaviour in confined environments as non-equilibrium particle effects dominate near walls. We adapt an extended hydrodynamic model for granular flows, which uses a density-gradient dependent “volume diffusion” term to correct the viscous stress tensor and heat flux, to simulate the shearing of a granular gas between two rough walls, and with corresponding boundary conditions. We use our Volume Diffusion (VD) model to predict channel flows for a range of mean volume fraction $\bar{\phi} = 0.01\text{--}0.4$, and inter-particle coefficients of restitution $e = 0.8$ and 0.9 , and compare with Discrete Element Method (DEM) simulations and classical NSF equations. Our model is capable of predicting non-uniform pressure, volume fraction and granular temperature, which become more significant for cases with mean volume fraction $\bar{\phi} \sim 0.1$, in which we typically observe non-uniform peak density variations, and large volume fraction gradients.

1 Introduction

Granular flows are frequently encountered in many environmental and industrial processes, such as: avalanches and landslides [1, 2], powder bed fusion [3–5], and grain transport and storage [6, 7]. Despite being a commonly encountered phenomenon, accurate modelling of granular flows is still a challenging problem due to their complex rheological properties: at low shear rates, particles settle into an ordered solid-like structures, while at higher shear rates, they can flow like a fluid [8–10]. Researchers have identified how liquid-like properties can be observed for

shearing high volume fraction flows, i.e., when the ratio of mean flow density to the solid particle density, $\bar{\phi}$, is between 0.4 and 0.6. The flows can then be modelled with continuum fluid methods [2, 8, 9].

As volume fraction, $\bar{\phi}$, decreases ($\lesssim 0.4$), particles undergo binary collisions [8, 9, 11], and the granular flow exhibits more gas-like properties. Sela and Goldhirsch [12] and Garzó and Dufty [13] investigated the fluid properties of a granular gas using kinetic theory, assuming inelastic particle collisions controlled by the coefficient of restitution, e , and determined an equivalent set of transport coefficients, including: shear viscosity, bulk viscosity, and thermal conductivity. Granular gas fluid prop-

*k.dadzie@hw.ac.uk

erties differ from an ideal gas due to inelastic particle collisions as well as rotational inertia and particle roughness and size, all of which introduce energy dissipation modes not admitted in ideal gases [13–15]. Many studies have exploited gas-like behaviours to model the one-dimensional shearing of granular fluids undergoing inelastic collisions for smooth particles [16], rough particles [17–19], and flows confined between two parallel walls [20, 21]. Vescovi *et al.* [20] employed continuum Navier–Stokes–Fourier-like equations for granular flow modelling in a sheared channel with $\bar{\phi} \gtrsim 0.1$, however, they needed to fit the slip velocity using data from their Discrete Element Method (DEM) simulations in the more inelastic cases ($e > 0.7$), instead of the initially proposed boundary conditions derived by Richman [22] for rough walls, in order to obtain good agreement with volume fraction and granular temperature variations across the channel, highlighting the difficulties of continuum granular flow modelling near boundaries.

As the volume fraction decreases further, $\bar{\phi} \lesssim 0.1$, we enter the regime of non-equilibrium flows in confined spaces, which cannot be accurately modelled by existing continuum theories [23–29]. Particle-based methods may be used to model such flows, however, are computationally expensive with less wide-spread adoption in industries. In elastic gases, non-equilibrium effects of rarefaction nature are characterised by the Knudsen number, Kn , which is the ratio of particle mean free path to a characteristic length, e.g., the height of a micro-channel. Some noticeable effects of rarefaction typically occur in Knudsen layers (regions close to boundaries with thickness of order of the gas’ mean free path) where predictions of local density, velocity, and temperature variations fail [23, 25–27, 29, 30].

A classical example of deviation from classical continuum flow model predictions is the phenomenon of enhanced mass flow rate of pressure-driven micro-channel gas flows in the now famous Knudsen-minimum experiment [31], arising from enhanced slip velocities at higher Knudsen numbers $\text{Kn} > 1$, while the conventional Navier–Stokes–Fourier (NSF) fluid equations erroneously predicts a monotonically decreasing mass flow rate [27, 32]. A similar Knudsen minimum can be observed in granular channel flows by numerically solving the generalised Enskog equation for inelastic collisions, however, this phenomenon disappears as the ratio

of the channel height to particle diameter decreases and approaches unity, until the mass flow rate appears to be a solely monotonically increasing function of Kn [24]. Following from this example, continuum-based models are expected to poorly capture non-equilibrium behaviours dominating granular gas flows even in straightforward configurations.

To overcome the inadequacies of the NSF equations (which strictly is only valid for flows in thermodynamic equilibrium), the Volume Diffusion (VD) equations have been proposed, following Brenner’s bi-velocity theory [33], which introduce an additional *volume diffusion flux* term to account for the fact that compressible fluid flows achieve mechanical equilibrium much quicker than reaching thermodynamic equilibrium [34]. This flux term, which is dependent on the local density gradient, captures additional stresses and work done to the fluid, and VD hydrodynamics correct the stress tensor and heat flux which can more accurately capture localised non-equilibrium effects [23, 25–27, 35]. VD equations have been shown to provide better agreement over conventional NSF equations when comparing with experiments and Molecular Dynamics (MD) simulations of confined and non-equilibrium fluid flows, in configurations such as the pressure driven flow in micro-channels [27, 32], lid-driven cavities [25, 26], shock-waves (with asymmetric density variations) [35], and enhanced liquid flow-rates in carbon nanotubes [28].

In this work, we now adapt the VD equations to model the shearing of a granular flow confined between two rough walls, benchmarking against DEM simulations. We modify the existing VD equations to be suitable for modelling granular flows, using transport coefficients derived from kinetic theory [13, 16, 20], and reduce the equations to a series of ordinary differential equations with boundary-value constraints. We extend our DEM modelling into low density ranges, $\bar{\phi} < 0.1$, which have not been extensively investigated for granular flows, and demonstrate how our new model better captures non-uniform pressure, density, and granular temperature variations between the walls, as well as the normal and shear stresses acting on the walls when compared to the conventional NSF equation predictions.

The remainder of this article is organised into the following sections: in §2, we outline the channel geometry and our DEM simulation methodology; in §3 we derive

our shear flow model from the VD equations; in §4 we show results of our DEM simulations and VD model, and compare with the classical NSF equations. Finally, in §5, we summarise the findings of the article, and where this research could be further explored.

2 DEM simulations

We simulated a granular flow shearing between two parallel particle walls using the DEM software LIGGGHTS [36]. We modelled a quasi-two-dimensional channel with height, $H = 0.2475$ m, in the y direction, and length 0.5 m ($\approx 2H$), and 0.05 m thickness in the x and z -directions, respectively, as shown in Fig. 1. The channel was enclosed between two single-layer Face Centred Cubic (FCC) walls, where the bottom wall was kept stationary and the top wall moved with constant velocity U_w .

Periodic boundary conditions were used on the x and z domain faces, and the simulations were integrated through the velocity Verlet integration scheme [36], with a time-step $\Delta t = 10^{-5}$ s [11]. During the main production runs, granular particles were placed randomly within the channel walls to match a defined mean volume fraction, $\bar{\phi}$. The simulations were first run for 10^9 – $10^{10}\Delta t$, until they reached a steady-state in total system energy [20]. After this first run, the simulations were then run a further $5 \times 10^7\Delta t$, during which time we measured properties of the granular fluid locally across the channel width. This measurement period was chosen to be approximately 200τ , where $\tau = H/U_w$ is the characteristic shear-time, to ensure the observed DEM simulation profiles were in a stable configuration [11]. Along with mean volume fraction $\bar{\phi}$, the coefficient of restitution was varied by investigating two values for inter-particle collisions $e = 0.8$ and 0.9 . We chose not to model values below $e = 0.8$, as this was found to lead to mostly asymmetric flow profiles, which is beyond the scope of this work, although could be investigated in the future using VD modelling [37–39].

In DEM modelling, collision forces, $F_{i,j}$, between particles i and j are calculated by [36]:

$$F_{i,j} = k_n r_{i,j} - \gamma_n \dot{r}_{i,j}, \quad (1)$$

where $r_{i,j}$ and $\dot{r}_{i,j}$ are the radial separation distance and relative normal velocity between particles i and j , respectively. The normal stiffness, k_n , was set to 20 kN/m, and

the normal damping, γ_n , was calculated from the coefficient of restitution, e , as [36]:

$$\gamma_n = \sqrt{\frac{2k_n M}{1 + \left(\frac{\pi}{\ln e}\right)^2}}, \quad (2)$$

where $M = \rho_0 \pi d_0^3 / 6$ is the mass of each particle, assuming equal particle masses. We specified particle diameter as, $d_0 = 0.01$ m, and solid grain density, $\rho_0 = 2500$ kg/m³, and we neglected friction forces in collisions and tangentially acting stiffness and damping forces, which is equivalent to assuming perfectly smooth particles [15]. For simplicity, the wall particles were specified to have the same properties as the interior granular fluid, i.e. identical diameter d_0 , coefficient of restitution e , and grain density ρ_0 .

We measured macroscopic granular properties locally in “bins”, such as the granular temperature:

$$T = \frac{1}{3N} \left[\sum_{i=1}^N |(u_i - u)|^2 \right], \quad (3)$$

where u_i is velocity vector of a particle i [20], N is the total number of particles in the bin, and the mean mass flow velocity in the bin is found by:

$$u = \frac{1}{N} \sum_{i=1}^n u_i. \quad (4)$$

Temperature is often measured in Kelvin, however, granular temperature in Eq. (3) has units m²/s²; we will refer to the granular temperature simply as “temperature” from here on.

The virial stress tensor \mathbf{S} is obtained from the DEM simulations in each bin:

$$\mathbf{S} = \frac{1}{V} \left[\sum_i^N M (u_i - u) \otimes (u_i - u) + \frac{1}{2} \sum_i^N \sum_{j \neq i}^N r_{i,j} \otimes F_{i,j} \right], \quad (5)$$

where V is the bin volume.¹

In the DEM simulations, the thermodynamic pressure p , which is used to relate the volume fraction and granular

¹In DEM simulations, the stress tensor is sometimes measured as the negative of the formulation given in Eq. (5) [36]. Our definition of stress tensor in Eq. (5) is chosen to be consistent with the stress tensor used in the NSF and VD equations, given later in §3.

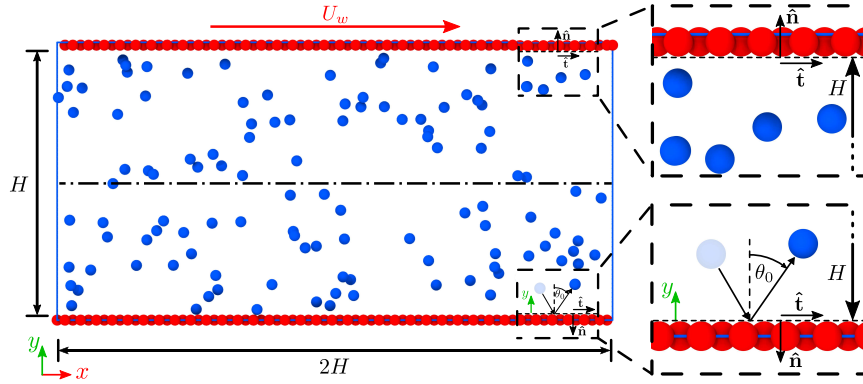


Figure 1: DEM simulation set-up. Wall particles are shown in red, while the granular flow particles are shown in blue. The insets show the upper and lower rough boundary walls in more detail, and the lower inset also shows the definition of contact angle, θ_0 , used in Eqs. (35) and (38) for slip and heat flux boundary conditions, respectively. The dot-dashed line shows the centreline of the channel, at $y = H/2$.

temperature, e.g. using the Carnahan–Starling (CS) radial distribution function [20, 40], can be estimated from the trace of the virial stress tensor [36]:

$$p = \frac{1}{3} (S_{xx} + S_{yy} + S_{zz}), \quad (6)$$

where S_{xx} , S_{yy} , and S_{zz} are the normal-face components of the stress tensor, in the x , y , and z directions, respectively.

3 Volume diffusion modelling for granular flows

Our new hydrodynamic model for granular flows is adapted from the Volume Diffusion (VD) model [23, 41]. This adaptation of VD equations for granular flows starts with the conservation of mass:

$$\frac{\partial \rho}{\partial t} + \nabla \cdot (\rho u) = 0, \quad (7)$$

where ρ is the flow density, and t is time. For a granular flow, density is more commonly expressed in terms of the grain density ρ_0 , and the flow volume fraction ϕ , i.e. $\rho = \rho_0 \phi$ [8, 20, 42, 43].

Next, we introduce the momentum transport equation

[23, 25–27, 35, 41]:

$$\frac{\partial (\rho u)}{\partial t} + \nabla \cdot (\rho u \otimes u) + \nabla \cdot [p\mathbf{I} + \Pi] = 0, \quad (8)$$

where \mathbf{I} is the identity tensor, and Π is the accompanying stress tensor, as given by:

$$\begin{aligned} \Pi = & -2\eta \left[\frac{1}{2} \left(\nabla(u - J_c) + \{ \nabla(u - J_c) \}^\top \right) \right. \\ & \left. - \frac{1}{3} \mathbf{I} \nabla \cdot (u - J_c) \right] - \rho J_c \otimes J_c - \eta_b \mathbf{I} \nabla \cdot (u - J_c), \quad (9) \end{aligned}$$

where η is the shear viscosity and η_b is the bulk viscosity, which have been derived by Garzó and Dufty [13] and listed in Appendix A, along with other fluid transport coefficients. The superscript \top in Eq. (9) indicates the transpose of the given vector or tensor. Note that the sum of the pressure and VD viscous stress tensor is equivalent to the virial stress tensor given in Eq. (5), for the DEM simulations, i.e. $p\mathbf{I} + \Pi = \mathbf{S}$.

In Eq. (9) appears the contribution of the volume diffusion flux, J_c , which arises from the kinetic level non-local equilibrium [41]. This volume diffusion flux for the granular fluid may be expressed as:

$$J_c = -k_m \frac{\nabla \rho}{\rho} = -k_m \frac{\nabla \phi}{\phi}, \quad (10)$$

which we elaborate on more below. The volume diffusivity coefficient, k_m , in Eq. (10) is expressed as [25–27]:

$$k_m = \alpha^* \text{Pr} \frac{\eta}{\rho_0 \phi}, \quad (11)$$

where α^* is a dimensionless constant, and $\text{Pr} = 5\eta/2\kappa$ is the Prandtl number for a granular gas. Note that Pr varies from the typical formulation for an ideal gas because of the change in units when granular temperature and thermal conductivity, κ , are used (see Eq. (16)). Previous investigations have found good agreement for gases using $\alpha^* = 1/3$ [25, 27], however, for liquids and denser media, this coefficient decreases [28, 44]. In the present granular simulations, we found the approximation $\alpha^* = (3g_0)^{-1}$ was sufficient, where g_0 is the radial distribution function [20, 40].

In VD theory, the velocity u used here (sometimes referred to as the mass velocity) describes the motion of the mass of the constituting particles, as in the continuity equation in Eq. (7). However, this is not necessarily the same as the velocity of the deformable fluid element that contains the mass of a group of particles, which is instead referred to as the volume velocity u_V [23, 27, 33, 34, 45]. The volume diffusion flux relates these two velocity terms by $J_c = u - u_V$, and accounts for additional macroscopic motion of fluid that occurs, despite no net motion of the fluid mass.

In its kinetic form, contributions from the volume diffusion flux to the constitutive equations are the direct consequence of molecular spatial stochasticity, not trivial in original kinetic equations such as the Boltzmann equation [46, 47]. We may also note that these density gradient terms (i.e. Korteweg-type stress tensor [45]) are the same ones obtained as quantum effects in the macroscopic continuum Navier–Stokes–Fourier equations when the Madelung equations are derived from the Schrödinger equation [48]. By setting $J_c = 0$ in Eq. (9), we obtain the classical form of the stress tensor used in the classical NSF granular model.

Continuing with our transport equations, the energy equation for the granular gas is here proposed as the energy equation from VD theory and complemented with energy dissipation from particle collisions [13, 23, 25, 27,

32, 35, 41, 46]. That is:

$$\begin{aligned} \frac{\partial}{\partial t} \left[\frac{1}{2} \rho u^2 + \frac{3}{2} \rho T \right] + \nabla \cdot \left[\frac{1}{2} \rho u^2 u + \frac{3}{2} \rho T u \right] \\ + \nabla \cdot [(p\mathbf{I} + \Pi) \cdot u] + \nabla \cdot J_u + \frac{\Gamma}{L} = 0, \quad (12) \end{aligned}$$

where Γ is the rate of energy dissipation from particle collisions [13], and L is the correlation length, a factor that accounts for increased particle collision frequency, when the assumption of molecular chaos breaks down, typically as local volume fraction increases, $\phi \gtrsim 0.4$ [20, 42, 43]. We employed the functional expression [42, 43]:

$$L = \begin{cases} 1, & L^* \leq 1 \\ L^*, & L^* > 1 \end{cases} \quad (13)$$

where:

$$L^* = \frac{1}{2} (\phi g_0)^{\frac{1}{3}} d_0 \frac{\partial u}{\partial y} T^{-\frac{1}{2}}. \quad (14)$$

The factor L^* is only relevant for a few of our high volume fraction cases, although we include it to obtain good agreement, especially for the peak volume fraction variations expected in the channel flow [20, 37–39]; our focus still remains on the non-equilibrium granular gas dynamics that become dominant for lower flow densities.

Continuing from Eq. (12), the energetic heat flux, J_u , is given by [23, 25–27, 41]:

$$J_u = q + pJ_c, \quad (15)$$

where the classical heat flux (or the Fourier equivalent heat flux) for a granular gas is given by [13]:

$$q = -\kappa \nabla T - \mu \nabla \phi, \quad (16)$$

and κ is the thermal conductivity. Note that this thermal conductivity refers to the macroscopic properties of the granular gas and not to the solid grain material composing individual particles. Additionally, since we consider granular temperature in this work given in Eq. (3) with units m^2/s^2 , the equivalent SI units of κ here are in Ws^2/m^3 . The second term in Eq. (16) contains a coefficient μ , that arises specifically in granular gases undergoing inelastic collisions, i.e. for $e < 1$, and is not present in an ideal gas [13, 49].

Eqs. (7), (8), (9), and (12) represent the VD hydrodynamic equations which account for the additional volume diffusion flux, J_c , on the stress tensor and local heat flux [23, 25–27, 30, 30, 35, 45]. By writing them in this form, we can simply obtain the classical NSF equations again, by setting $J_c = 0$, which will become useful in the analysis of our DEM and VD results presented in §4.

For our sheared granular flow cases, as described in §2, we assume a steady-state flow, i.e. $\partial/\partial t = 0$, and with variations only in the y -direction, i.e. $\partial/\partial x, \partial/\partial z = 0$. Only the x component velocity u is considered, so $u = [u(y) \ 0 \ 0]^\top$. Applying these assumptions, we write $J_c = [0 \ J_c(y) \ 0]^\top$ from Eq. (10), where $J_c(y)$ is the y component of J_c . The stress tensor in Eq. (9) then becomes:

$$\Pi = \begin{bmatrix} \left(-\frac{2\eta}{3} + \eta_b\right) \frac{\partial J_c}{\partial y} & -\eta \frac{\partial u}{\partial y} & 0 \\ -\eta \frac{\partial u}{\partial y} & \left(\frac{4\eta}{3} + \eta_b\right) \frac{\partial J_c}{\partial y} - \rho_0 \phi J_c^2 & 0 \\ 0 & 0 & \left(-\frac{2\eta}{3} + \eta_b\right) \frac{\partial J_c}{\partial y} \end{bmatrix}. \quad (17)$$

By considering Eqs. (8) and (17) in the x direction, we denote the xy shear stress component of the VD virial stress tensor in Eq. (9) as $s = -S_{xy}$, which is constant, i.e. $\partial s/\partial y = 0$, and:

$$s = \eta \frac{\partial u}{\partial y}. \quad (18)$$

Similarly, in the y direction, we extract:

$$p + \left(\frac{4\eta}{3} + \eta_b\right) \frac{\partial J_c}{\partial y} - \rho_0 \phi J_c^2 = S_{yy}, \quad (19)$$

where S_{yy} is a constant, i.e. $\partial S_{yy}/\partial y = 0$. However, unlike in previous analyses [15–17, 20], we find that the pressure p is *not* constant, owing to the volume diffusion flux, and is related to density and granular temperature by:

$$p = fT, \quad (20)$$

where $f = \rho_0 \phi [2g_0 \phi (1 + e) + 1]$. We emphasise here, that it is important to distinguish between the normal stress S_{yy} , and the thermodynamic pressure p , since the normal stress is the physical force per unit area exerted on the particles within the channel and on the walls. The thermodynamic pressure accounts for the stress arising from the

thermal or kinetic energy of the particles, from Eq. (20), however, as we will see in §4, only partially contributes to the total normal stress, and instead we must consider the additional stress from the volume diffusion flux terms, see Eq. (19), to accurately capture this normal stress profile. Still, we must carefully consider the thermodynamic pressure in our modelling, since it relates important thermodynamic properties together, such as volume fraction and temperature, particularly in high volume fraction cases, where the assumption of molecular chaos breaks down [20, 42, 43].

We employ the radial distribution function proposed by Vescovi *et al.* [20], which is suitable for high volume fraction cases $\phi > 0.4$, and highly inelastic collisions $e < 0.95$:

$$g_0(\phi) = \begin{cases} g_{0CS}(\phi), & \text{for } \phi \leq \phi_m \\ \psi g_{0CS}(\phi) + \frac{2(1-\psi)}{\phi_{rcp} - \phi}, & \text{for } \phi > \phi_m \end{cases}, \quad (21)$$

where $g_{0CS}(\phi) = (2 - \phi)/2(1 - \phi)^3$ is the CS radial distribution function [40], and:

$$\psi = \frac{\phi^2 - 2\phi_m \phi + \phi_{rcp}(2\phi_m - \phi_{rcp})}{2\phi_{rcp}\phi_m - \phi_m^2 - \phi_{rcp}^2}, \quad (22)$$

where $\phi_{rcp} = 0.636$, $\phi_f = 0.49$, and $\phi_m = 0.4$, are the random close packing limit for hard spheres, volume fraction at “freezing” point, and volume fraction at “merging” point, respectively [20]. In Appendix B, we verify that the radial distribution function given in Eq. (21) is suitable for our work, using data from DEM simulations with imposed Lees–Edwards (LE) boundary conditions [36, 50].

Continuing our derivation, by reducing Eq. (12), we obtain:

$$s \frac{\partial u}{\partial y} = \frac{\partial q}{\partial y} + \frac{\partial}{\partial y} (pJ_c) + \frac{\Gamma}{L}, \quad (23)$$

and heat flux is simplified from Eq. (16):

$$q = -\kappa \frac{\partial T}{\partial y} - \mu \frac{\partial \phi}{\partial y}, \quad (24)$$

Eq. (20) is differentiated, and rearranged along with Eqs. (18)–(20), (23), and (24). The full VD hydrodynamic equations for our granular flow configuration, reduced into a set of differential equations, then become as fol-

lows:

$$\frac{\partial u}{\partial y} = \frac{s}{\eta}, \quad (25)$$

$$\frac{\partial p}{\partial y} = \frac{J_c \phi}{k_m} \left(\frac{f \mu}{\kappa} - \frac{\partial f}{\partial \phi} \frac{p}{f} \right) - \frac{f}{\kappa} q, \quad (26)$$

$$\frac{\partial \phi}{\partial y} = -\frac{J_c \phi}{k_m}, \quad (27)$$

$$\frac{\partial J_c}{\partial y} = (S_{yy} + \rho_0 \phi J_c^2 - p) \left(\frac{4\eta}{3} + \eta_b \right)^{-1}, \quad (28)$$

and:

$$\frac{\partial q}{\partial y} = \frac{s^2}{\eta} - p \frac{\partial J_c}{\partial y} - J_c \frac{\partial p}{\partial y} - \frac{\Gamma}{L}. \quad (29)$$

In order to compare with classical NSF equations, we set J_c , $\partial p / \partial y$, $\partial J_c / \partial y = 0$, to obtain a set of alternative differential equations for NSF modelling, and Eqs. (27) and (29) are instead replaced with:

$$\frac{\partial \phi}{\partial y} = q \left(\frac{\kappa}{f} \frac{\partial f}{\partial \phi} T - \mu \right)^{-1}, \quad (30)$$

and

$$\frac{\partial q}{\partial y} = \frac{s^2}{\eta} - \frac{\Gamma}{L}, \quad (31)$$

respectively [20], while Eq. (25) is used as before, and $p = S_{yy}$.

To ensure both the VD and NSF models achieve a target mean density $\bar{\phi}$, which is chosen to match each case from our DEM simulations, we introduce the term $m = \int_0^y \phi dy$ [20], such that:

$$\frac{\partial m}{\partial y} = \phi. \quad (32)$$

Eqs. (25)–(32) are now in the form of six explicit differential equations that can be solved. We must also obtain two additional parameters s and S_{yy} , making a total of eight boundary conditions necessary to fully close the problem. We employ boundary conditions proposed by Nott [15] for smooth inelastic particles, to estimate slip velocity u_s and wall heat flux q_w . The flux of linear mo-

mentum to the wall Λ_w is given by [15]:

$$\begin{aligned} \Lambda_w = & \rho_0 \phi g_w T \hat{n} + \frac{2\sqrt{2}}{3\sqrt{\pi}} \rho_0 \phi g_w T^{1/2} \mathbf{P} \cdot u_s \\ & - \frac{1}{3} \rho_0 d_0 T g_w \mathbf{P} \cdot \nabla \phi \\ & - \rho_0 d_0 g_w \left[\frac{5}{96\sqrt{2}g_0} \left(1 + \frac{12}{5} G \right) + \frac{\phi}{3} \right] \mathbf{P} \cdot \nabla T \\ & - \rho_0 d_0 T^{1/2} g_w \left[\frac{5\sqrt{\pi}}{96g_0} \left(1 + \frac{8}{5} G \right) \mathbf{Q} + \frac{2\sqrt{2}\phi}{\sqrt{\pi}} \mathbf{R} \right] : \nabla u, \end{aligned} \quad (33)$$

where $u_s = u - U_w$ is the slip velocity vector, U_w is the wall velocity vector, $G = \phi g_0$, and g_w is a factor which quantifies the increase in volume fraction due to particles in contact with the wall, compared to that of the bulk [10, 15], and is given in Table A1. We have omitted rotational flux terms, which are only relevant for rough particles [15]. Coefficients \mathbf{P} , \mathbf{Q} , and \mathbf{R} , are given by:

$$\mathbf{P} = \frac{2(1 - \cos^3 \theta_0)}{\sin^2 \theta_0} \hat{n} \hat{n} + \left[2(1 + \cos \theta_0)^{-1} - \cos \theta_0 \right] \hat{i} \hat{i}, \quad (34a)$$

$$\begin{aligned} \mathbf{Q} = & \left(\frac{1}{3} + \cos^2 \theta_0 \right) \hat{n} \hat{n} + \frac{1}{2} \sin^2 \theta_0 (\hat{i} \hat{n} + \hat{i} \hat{n}) \\ & - \left(\frac{1}{6} + \frac{1}{2} \cos^2 \theta_0 \right) \hat{n} \hat{i}, \end{aligned} \quad (34b)$$

$$\mathbf{R} = \frac{1}{2} (1 + \cos^2 \theta_0) \hat{n} \hat{n} + \frac{1}{4} \sin^2 \theta_0 (\hat{i} \hat{n} + \hat{i} \hat{n} + \hat{n} \hat{i}), \quad (34c)$$

respectively, where θ_0 is the maximum angle that a particle can subtend normal to the wall, pertained by the wall's roughness [15, 22], and unit vectors \hat{n} and \hat{i} , are the normal and tangential flow (following x) directions, respectively (see insets in Fig. 1). Note vector \hat{n} points outwards from the wall, i.e. away from the channel. Unit vectors in the tangential z direction have not been given in Eq. (34) to improve clarity, however, can be found in Nott [15].

For our shear flow case, considering only the linear shear stress in the x direction, i.e. s , we can rearrange

Eq. (33) in terms of the x component slip velocity:

$$u_s = \pm s(1 + \cos \theta_0) \times \frac{\left(1 - \frac{1}{2} \sin^2 \theta_0 \frac{\rho_0 d_0 T^{1/2} g_w}{\eta} \left\{ \frac{5\sqrt{\pi}}{96g_0} \left(1 + \frac{8}{5} \phi g_0\right) + \frac{\sqrt{2}\phi}{\sqrt{\pi}} \right\}\right)}{\frac{2\sqrt{2}}{3\sqrt{\pi}} \rho_0 \phi g_w T^{1/2} (2 - (1 + \cos \theta_0) \cos \theta_0)}, \quad (35)$$

where the positive and negative signs correspond to the lower and upper walls, respectively. We determine θ_0 by fitting Eq. (35) to our DEM results, using measured shear stress and slip velocity at the wall, as shown in Fig. 2. For simplicity, we fit a single mean value of $\theta_0 = (0.67 \pm$

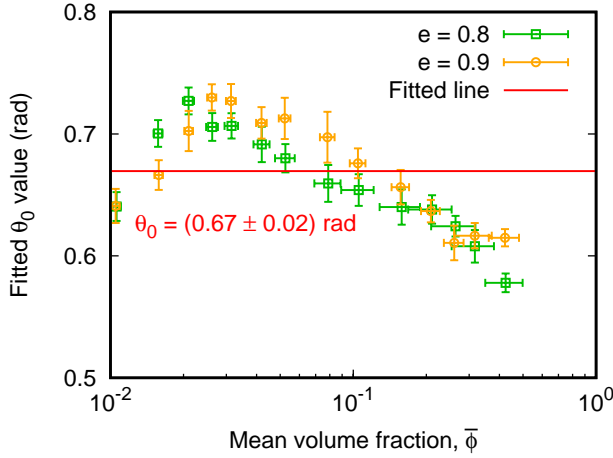


Figure 2: Variation in values of θ_0 , found by fitting Eq. (35) to our DEM simulations, for different coefficients of restitution, e , and the solid line shows the mean value of all cases.

0.02)rad for all the cases, which is approximately equal to the value of $\pi/5$ obtained analytically in other works [20].

Temperature is usually constrained in rarefied gas modelling through a first-order “jump” boundary condition [25, 26, 29], or alternatively, the case may be assumed isothermal to simplify the analyses [27, 44]. However, in a DEM simulation, temperature is not trivial to determine for a rough granular wall, and the “thermostatting” approaches often used in MD simulations do not work well

in DEM. Here we apply the wall heat flux model boundary conditions from Nott [15]:

$$\hat{n} \cdot q = \Upsilon_w - \Lambda_w \cdot u_s, \quad (36)$$

where:

$$\Upsilon_w = \left(\frac{2}{\pi}\right)^{1/2} (1 + \cos \theta_0)^{-1} (1 - e^2) \rho_0 \phi g_w T^{3/2}, \quad (37)$$

is the rate of kinetic energy dissipation at the wall per unit area due to inelastic collisions. For our case, we simplify Eq. (36), and equate Eq. (33) to the normal stress at the wall, S_{yy} , to obtain two sets of boundary conditions, for heat flux, q_w , and volume diffusion flux, $J_{c,w}$, respectively, at the walls:

$$q_w = \pm (-\Upsilon_w + s |u_s|), \quad (38)$$

and

$$J_{c,w} = \frac{\pm (S_{yy} - \rho_0 \phi g_w T) + \frac{A}{\kappa} q_w}{\frac{A\mu\phi}{\kappa k_m} - \frac{B\phi}{k_m}}, \quad (39)$$

where the positive and negative signs of (\pm) correspond to the lower and upper boundaries, respectively, and coefficients A and B are derived from the tensors in Eq. (34):

$$A = \rho_0 d_0 g_w \left[\frac{5}{96\sqrt{2}g_0} \left(1 + \frac{12}{5}G\right) + \frac{\phi}{3} \right] \frac{2(1 - \cos^3 \theta_0)}{\sin^2 \theta_0}, \quad (40)$$

and

$$B = \frac{1}{3} \rho_0 d_0 T g_w \frac{2(1 - \cos^3 \theta_0)}{\sin^2 \theta_0}, \quad (41)$$

respectively.

Additionally, Eq. (32) has boundary conditions [20]:

$$m(y=0) = 0, \quad (42a)$$

$$m(y=H) = \bar{\phi}H, \quad (42b)$$

which satisfies the mean volume fraction in the channel. Eqs. (35), (39), (38), and (42) now provide sufficient boundary conditions to fully solve for our VD model in Eqs. (25)–(32), with additional parameters s and S_{yy} .

4 Results and Discussions

We solved Eqs. (25)–(29) and (32), with boundary conditions defined by Eqs. (35), (38)–(42), using the BVP4C

solver function in MATLAB [51], and compared results to our DEM simulations. For validations, we determined the conventional NSF solution, by solving Eqs. (25), and (30)–(32), while using the same rough wall boundary conditions in Eqs. (35), (38), and (42).

Fig. 3 shows the variations in volume fraction, ϕ , normalised velocity, u/U_w , and normalised temperature, T/U_w^2 , across the channel for the $\bar{\phi} = 0.32, 0.211$, and 0.11 cases, where the VD model gives a general improvement over the NSF model.² The VD equations typically result in higher peak volume fractions near the centreline ($y/H = 0.5$), greater slip velocities, and lower granular temperatures. In Fig. 3, we have also plotted the results predicted by the Navier–Stokes–Fourier models under Lees–Edwards (LE) boundary conditions [50], where shear flow is imposed through the displacement of the y periodic faces [36], and no rough walls. These are solved using the same differential equations as the NSF solution, however, assuming no slip and no heat transfer at the boundaries (adiabatic walls), i.e. $u_s = 0$ and $q_w = 0$, respectively, which are also the assumptions in models proposed by Lun *et al.* [16] and Chialvo and Sundaresan [19].

Our VD model generally provides better agreement over the NSF models for the above cases with $\bar{\phi} \sim 0.1$, which occurs since there are large volume fraction gradients, which means the volume diffusion flux term, J_c , becomes more significant, from Eq. (10). For lower volume fraction cases $\bar{\phi} \lesssim 0.05$, the volume fraction profiles became more uniform across the channel wall, and the VD and NSF solutions tend to show similar results, as shown in Fig. 4. Alam *et al.* [39] found qualitatively similar results, albeit assuming adiabatic walls: for low $\bar{\phi}$, the volume fraction across the channel is uniform, however, as $\bar{\phi}$ increases, layering instabilities dominate the flow profile, giving rise to the peak density variations [37–39], which we see in our DEM simulations, and this is consistent with our VD model which shows the greatest deviations with the NSF model for higher mean volume fractions $\bar{\phi} \sim 0.1$.

Our VD model also better predicts the stresses for these cases, compared to the classical Navier–Stokes–Fourier equations, as shown in Fig. 5, for various volume fractions at $e = 0.8$. The normal stress, S_{yy} , and pressure, p ,

are measured in the DEM results using Eqs. (5) and (6), respectively. Crucially, we can see the non-uniform variation in pressures in the DEM and VD model results in Figs. 5(a), (d), and (g), which are not captured by the conventional NSF equations. Instead, it is the normal y -stress tensor component, S_{yy} , and the shear stress s in Figs. 5(b), (e), and (h), which remain constant across the channel as expected from Eqs. (19) and (25), respectively. To further demonstrate the difference between measured stress tensor and pressure profiles, we have plotted the normal x and z stress tensor components in Figs. 5(c), (f), and (i), obtained from the thermodynamic pressure and the stress tensor elements in Eq. (17):

$$S_{xx} = S_{zz} = p + \left(-\frac{2\eta}{3} + \eta_b \right) \frac{\partial J_c}{\partial y}. \quad (43)$$

Again, we show clearly non-uniform variations in the stresses S_{xx} and S_{zz} , while the NSF solution predicts constant values (since there is no volume diffusion flux terms). However, contrary to what we expected from the VD stress tensor in Eq. (17), the S_{xx} and S_{zz} stresses are not exactly equal in our DEM simulations, with the normal x component consistently larger than the z component by around 0.1 (normalised by $\rho_0 U_w^2 (d_0/H)^2$). This is likely because we only considered volume fraction gradients in Eq. (10), however, other gradient terms, such as in thermodynamic pressure and temperature, are also theorised to contribute to the volume diffusion flux [28, 44, 45], and these quantities are clearly non-uniform in our cases here. Introducing more volume diffusion flux terms is challenging, as we would also have to introduce more necessary boundary conditions to close the problem, so for the purposes of this work, we limited ourselves to capturing volume diffusion flux driven by volume fraction gradients only.

In Fig. 6(a)–(c), we show the variation in stresses against volume fraction for the VD, NSF, and NSF with LE boundary condition models, for $e = 0.9$ and 0.8, respectively. The NSF model captures s and S_{yy} at low ($\bar{\phi} \sim 0.01$) volume fractions, and is in generally good agreement with our VD model. However, as we discussed earlier, for $\bar{\phi} \gtrsim 0.05$, the conventional NSF solutions deviate from our VD model, which occurs for cases where there were large density gradients (see Fig. 3), most prominently at $\bar{\phi} \sim 0.1$, and volume diffusion flux becomes relevant. This disagreement continues for further

²For the remainder of this article, results for the velocity, temperature, volume diffusion flux, and stresses are normalised by U_w , U_w^2 , U_w , and $\rho_0 U_w^2 (d_0/H)^2$, respectively.

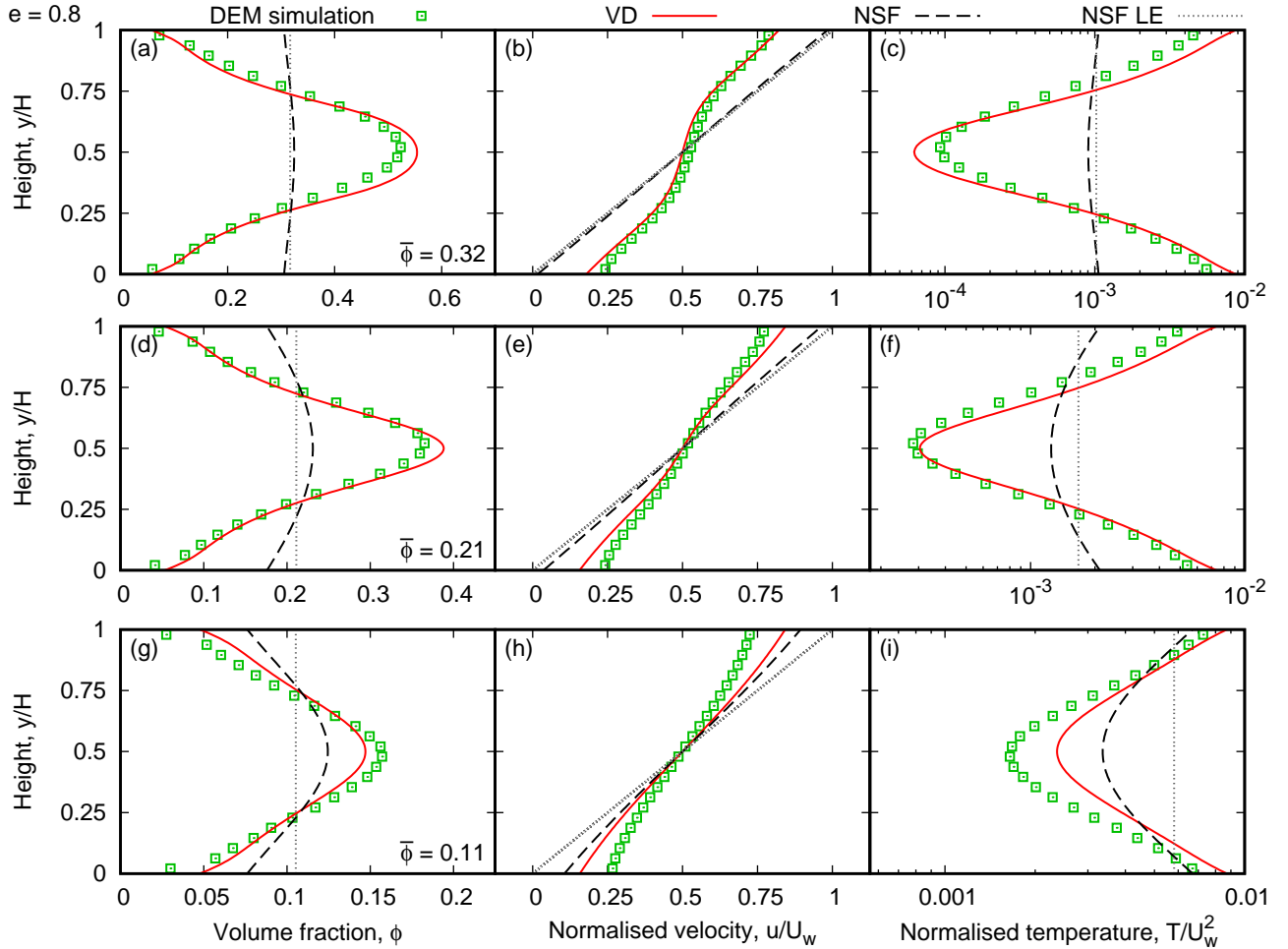


Figure 3: Variation in volume fraction, ϕ , velocity, u/U_w , and temperature, T/U_w^2 , in the: (a)–(c) $\bar{\phi} = 0.32$, (d)–(f) $\bar{\phi} = 0.211$, and (g)–(i) $\bar{\phi} = 0.11$ cases, all for $e = 0.8$.

increases of $\bar{\phi}$, until we reach the maximum random close packing limit ϕ_{rcp} , which is the maximum physical case we can explore in either the NSF or VD models.

As we discussed above, the VD and NSF equations converged on similar solutions for $\bar{\phi} \sim 0.01$, since the volume fraction profiles became more uniform across the channel. This explains a unique finding in our VD modelling, in comparison with previous applications of VD theory. VD equations, and general bi-velocity methods, have previously been used to model rarefied gas dynamics, generally showing greater effects as Kn increases,

typically above unity, for low-density cavity flows and pressure-driven micro-channel flows [25–27]. In our current simulations, we express Knudsen numbers in the configurations as $Kn = d_0/(6\sqrt{2}\bar{\phi}H)$ [25–27, 29] which applies to the NSF and VD channel models only, where the flow is confined between two walls. However, the NSF and VD equations show almost complete agreement as Kn approaches unity, and instead the largest deviation occurs at $Kn \sim 0.01$, or approximately $\bar{\phi} \sim 0.1$, where layering instabilities result in a peak density variation, which develop the density gradient dependent volume diffusion

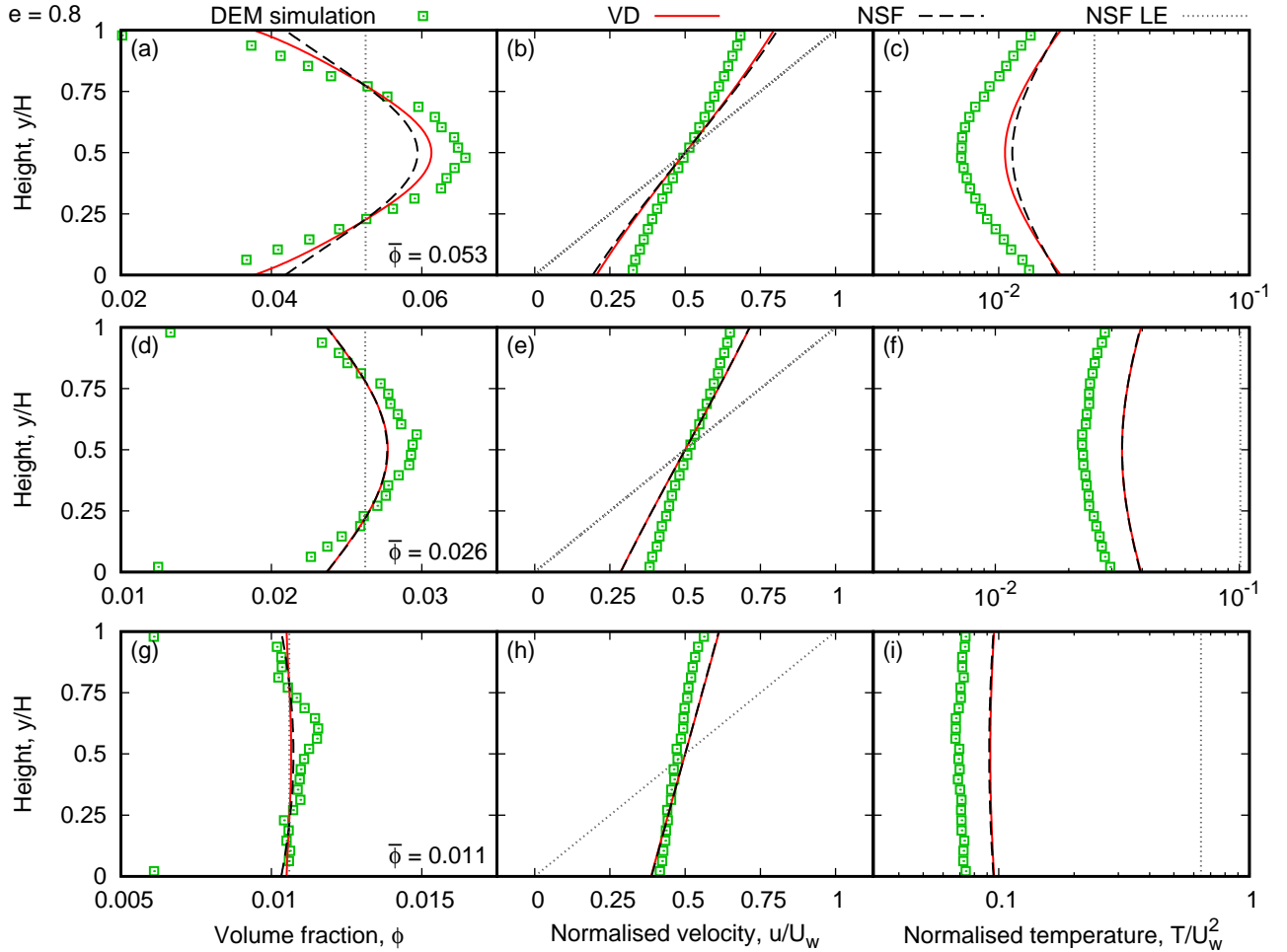


Figure 4: Variation in volume fraction, ϕ , velocity, u/U_w , and temperature, T/U_w^2 , in the: (a)–(c) $\bar{\phi} = 0.053$, (d)–(f) $\bar{\phi} = 0.026$, and (g)–(i) $\bar{\phi} = 0.011$ cases, all for $e = 0.8$.

flux terms in the VD equations. We conclude that in this granular shearing case, the Knudsen number does *not* play a significant role after all, and we should focus on cases where volume fraction gradients are more significant, which might not necessarily occur in rarefied flows.

Despite the deviations between the VD and NSF models, Fig. 6 shows that both models give similar qualitative agreements with the DEM results, when looking at normal and shear stresses, however, as we showed previously in Figs. 3 and 5, the VD model is able to provide better detail for the non-uniform varying properties within the

channel, such as volume fraction and temperature, and also thermodynamic pressure variations which the NSF model cannot capture.

The differences between the NSF and VD models seem weakly dependent on the coefficient of restitution, as shown in Figs. 6(a)–(c) for $e = 0.9$ and 0.8 cases, respectively. For each value of e , we see close agreement between the NSF and VD models at low volume fraction $\bar{\phi} \sim 0.01$, with deviations between the two models generally increasing as $\bar{\phi}$ increases, due to the larger volume fraction gradients. This suggests that any discrepancies

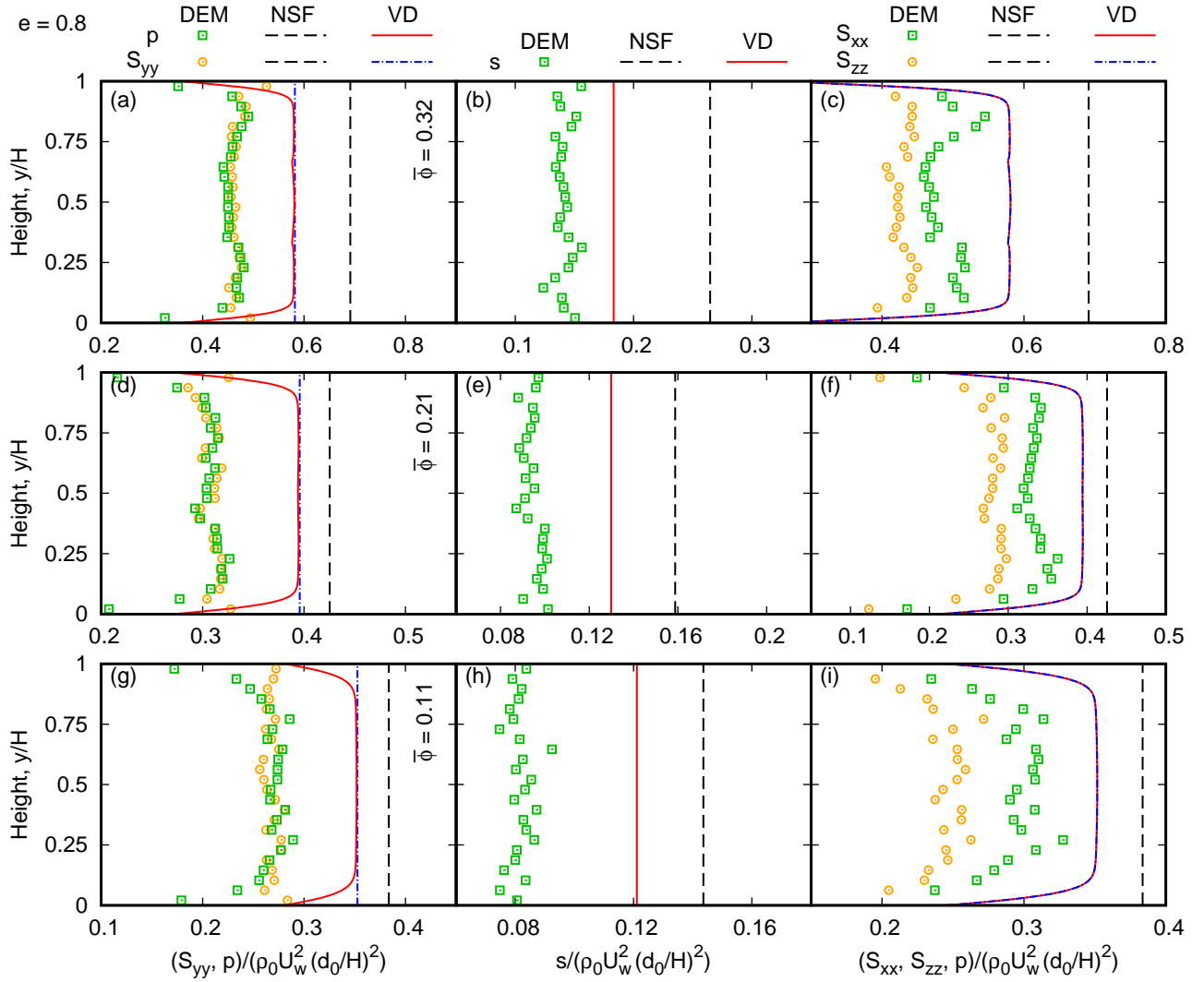


Figure 5: Variation in normal stress component, S_{yy} and pressure, p , shear stress, s , and x and z normal stresses, S_{xx} and S_{zz} , respectively, in the: (a)–(c) $\bar{\phi} = 0.32$, (d)–(f) $\bar{\phi} = 0.21$, and (g)–(i) $\bar{\phi} = 0.11$ cases, all for $e = 0.8$. The legends above (a), (b), and (c) apply to all subfigures in the same column.

in the NSF for shear flow modelling are less dependent on particle inelasticity, so long as a peak volume fraction variation occurs, which still occurs in elastic particle interactions [29].

We find that both the NSF and VD tend to overpredict stresses in the DEM simulations for the low volume frac-

tion cases $\bar{\phi} \sim 0.01$, which becomes more apparent as e decreases, however, we also find that the NSF model with LE boundary conditions also overpredicts stresses in this range, as shown in Appendix B. From this additional comparison, we suggest that the disagreement most likely arises from the fluid transport coefficients used

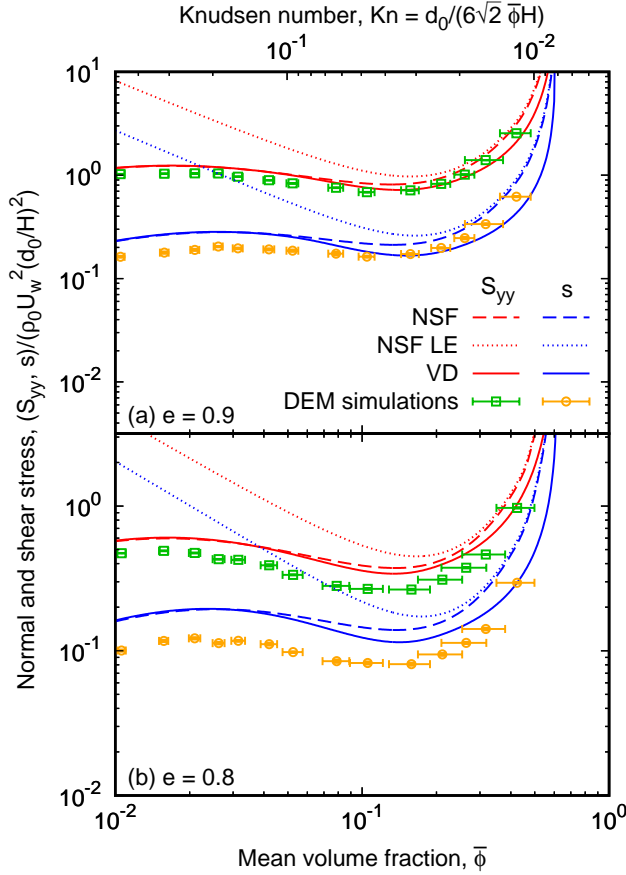


Figure 6: Variation in normal stress, S_{yy} and shear stress, s , for the NSF and VD and NSF (with LE boundary condition) models, for the (a) $e = 0.9$ and (b) $e = 0.8$ cases. The Knudsen number, Kn , applies only to the NSF and VD channel models, i.e. with rough walls. The legend in (a) also applies to (b) and (c).

here, rather than our use of VD modelling or choice of boundary conditions in §3.

We also note that the value of θ_0 in Fig. 2, used to determine slip velocity in Eq. (35), and energy dissipation rate at the wall in Eq. (37), appeared to decrease with increasing volume fraction, which could have affected agreement with our DEM results. It may seem unusual that θ_0 is not necessarily constant, as one might assume θ_0 is a purely

geometric parameter, relating to the wall's FCC structure [15, 20, 22]. However, the coefficient of restitution and volume fraction have previously been shown to alter the mean collision-angle distribution in inelastic particle collisions [21], and we suggest this could also be occurring at the walls in our cases. We expect for the dilute ($\bar{\phi} \rightarrow 0$) cases, θ_0 would tend to a constant value; however, for increasing local volume fraction, dense layered microstructures form [21], which break down the assumption of molecular chaos, and the collision angle at the wall θ_0 would naturally become dependent on the surrounding high density of particles.

5 Conclusions

We have adapted the Volume Diffusion (VD) extended hydrodynamic equations to model the shearing of a granular flow confined between two walls, using gas properties obtained from kinetic theory for inelastic particles [13]. We compared our new VD model to Discrete Element Method (DEM) simulations for granular flow contained between two rough shearing walls, where we varied mean volume fraction $\bar{\phi}$ and the inelasticity of inter-particle collisions, through the coefficient of restitution e . The VD equations included a volume fraction (or normalised density) gradient term, the *volume diffusion flux*, J_c , which better captured the volume fraction and granular temperature profiles across the channel, when compared to the classical Navier–Stokes–Fourier (NSF) equations. We employed boundary conditions for slip-velocity and heat flux, commonly used in granular flow literature [15], and derived a new set of boundary conditions for the volume diffusion flux, by equating the normal stress at the upper and lower walls with the VD stress tensor. Our VD model provided good agreement with DEM simulations for predicting local volume fraction, flow velocity, and granular temperature, and was able to capture non-uniform variations in pressure and stresses, unlike the classical NSF equations.

Contrary to what we expected from previous investigations [25–27], we found that VD equations were weakly dependent on Knudsen number Kn approaching unity and beyond, giving very similar results to NSF equations. This results from low the volume fraction cases producing near-uniform density across the channel for $\bar{\phi} \lesssim 0.05$ [37–39], as found in our DEM simulations. Increasing

the mean volume fraction in our simulations introduced layering instabilities for $\bar{\phi} \sim 0.1$, which resulted in peak volume fraction variations in the channel, and where the volume diffusion flux terms became most significant, resulting in the regime where we saw the greatest deviations between our VD model and the classical NSF equations.

Our derived VD model only considered the volume diffusion flux from density gradients, however, gradients in temperature and thermodynamic pressure can also induce volume diffusion flux terms, that could account for some of discrepancies in our normal and shear stress results [28, 44, 45]. Adapting the model to account for these additional VD flux terms would also require more necessary boundary conditions, and likely modifications to the existing velocity slip and heat flux boundary conditions, which may partly explain the variation of particle-wall collision angle θ_0 with local volume fraction we observed in our DEM simulation results. We assumed perfectly smooth particles whereas more physically relevant granular systems in nature and engineering often contain rough particles, with finite inter-particle friction, and non-uniform size. These can be implemented for better applications for the experimental validations [15, 17–19]. Future work could also further investigate the application of the VD equations for modelling asymmetric flow behaviour, which becomes more prevalent at lower values of e [37–39].

Acknowledgements

This work is supported in the UK by the Engineering and Physical Sciences Research Council (EPSRC) under grant EP/R007438/1.

A Transport coefficients for a granular gas

Table A1 gives the transport coefficients, approximating a granular medium as a gas [13], and using the radial distribution function defined in Eqs. (21) and (22). Coefficients denoted by the asterisk (*) superscript are given in dimen-

sionless form, and can be related by:

$$\eta^* = \eta/\eta_0, \quad (\text{A1a})$$

$$\eta_b^* = \eta_b/\eta_0, \quad (\text{A1b})$$

$$\kappa^* = \kappa/\kappa_0, \quad (\text{A1c})$$

$$\mu^* = \mu\phi/T\kappa_0, \quad (\text{A1d})$$

$$\zeta^* = \Gamma/(3\rho_0\phi T v_0/2), \quad (\text{A1e})$$

where:

$$\eta_0 = \frac{5}{96}\rho_0\pi^{1/2}d_0T^{1/2}, \quad (\text{A2})$$

and:

$$\kappa_0 = \frac{15}{4}\eta_0, \quad (\text{A3})$$

are the low-volume fraction values of shear viscosity and thermal conductivity, respectively, in the elastic limit ($e = 1$) [13]. Additionally, the characteristic collision frequency is given by:

$$v_0 = \rho_0\phi T/\eta_0. \quad (\text{A4})$$

B Lees–Edwards boundary conditions

In this appendix, we show results of our DEM simulations under Lees–Edwards (LE) boundary conditions, which were set up in a fully periodic box, with dimensions 0.5 m, 0.25 m, and 0.05 m, in the x , y , and z dimensions, respectively, and run for $10^7\Delta t$ to reach a steady-state and $10^8\Delta t$ for averaging. Eq. (21) provides a better fit than the Carnahan–Starling (CS) radial distribution function [40], particularly at $\bar{\phi} > 0.4$, as shown in Fig. B1. We also see no significant effect of e on g_0 .

Fig. B2 shows the variation in normal and shear stresses inside the channel under LE boundary conditions, which are in good agreement with the NSF equations. Since no density fluctuations were present, due to the absence of walls in LE boundary conditions, there is no difference between the NSF and VD equations solutions, and therefore $p = S_{yy}$.

Table A1: Fluid transport coefficients for a granular gas [13, 15].

$$\begin{aligned}
 G &= \phi g_0, \\
 g_w &= 1 + 4G, \\
 F &= \frac{1+e}{2} + \frac{1}{4G}, \\
 \eta^* &= \eta^{k*} \left[1 + \frac{4}{5}G(1+e) \right] + \frac{3}{5}\eta_b^*, \\
 \eta^{k*} &= \left(v_\eta^* - \frac{1}{2}\zeta^* \right)^{-1} \left[1 - \frac{2}{5}G(1+e)(1-3e) \right], \\
 c^* &= 32(1-e)(1-2e^2) [81 - 17e + 30e^2(1-e)]^{-1} \\
 \eta_b^* &= \frac{128}{5\pi} \phi G(1+e) \left(1 - \frac{1}{32}c^* \right), \\
 \kappa^* &= \kappa^{k*} \left[1 + \frac{6}{5}G(1+e) \right] + \frac{2304}{225\pi} \phi G(1+e) \left(1 + \frac{7}{32}c^* \right), \\
 \kappa^{k*} &= \frac{2}{3} (v_\kappa^* - 2\zeta^*)^{-1} \left(1 + \frac{1}{2}(1+4FG)c^* + \frac{3}{5}G(1+e)^2 \left\{ 2e - 1 + \left[\frac{1}{2}(1+e) - \frac{5}{3(1+e)} \right] c^* \right\} \right) \\
 \mu^* &= \mu^{k*} \left[1 + \frac{6}{5}G(1+e) \right], \\
 \mu^{k*} &= 2(2v_\mu^* - 3\zeta^*)^{-1} \left[(1 + \phi \partial_\phi \ln g_0) \zeta^* \kappa^{k*} + \frac{4FG}{3} (1 + \phi \partial_\phi \ln \{4FG\}) c^* \right. \\
 &\quad \left. - \frac{4}{5}G \left(1 + \frac{1}{2}\phi \partial_\phi \ln g_0 \right) (1+e) \left\{ e(1-e) + \frac{1}{4} \left[\frac{4}{3} + e(1-e) \right] c^* \right\} \right], \\
 \zeta^* &= \frac{5}{12}g_0(1-e^2) \left(1 + \frac{3}{32}c^* \right),^a \\
 v_\eta^* &= g_0 \left[1 - \frac{1}{4}(1-e)^2 \right] \left[1 - \frac{1}{64}c^* \right], \\
 v_\kappa^* = v_\mu^* &= \frac{1}{3}(1+e)g_0 \left[1 + \frac{33}{16}(1-e) + \frac{19-3e}{1024}c^* \right]
 \end{aligned}$$

^a We have neglected the divergence term in the dimensionless dissipation rate ζ^* , from Ref. 13.

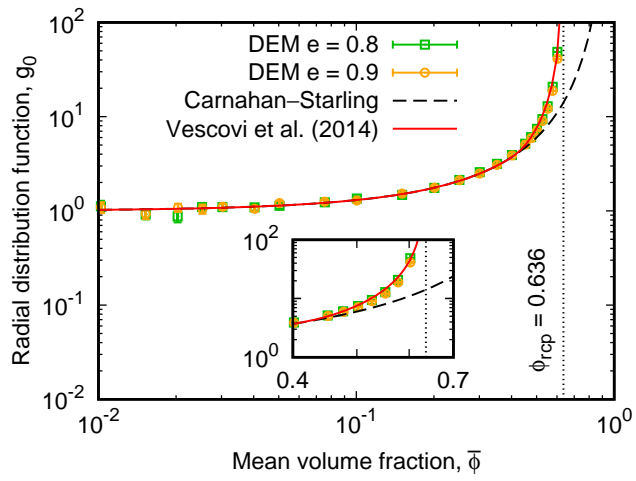


Figure B1: Variation in radial distribution function, g_0 , with mean volume fraction, $\bar{\phi}$, from the DEM simulations, and predicted using Eqs. (21) and (22) proposed by Vescovi *et al.* [20], with comparisons to the Carnahan–Starling radial distribution function [40]. The dotted line shows the maximum possible volume fraction, at the random close packing limit ϕ_{rcp} , and the inset shows results for higher volume fractions $\phi > 0.4$ in more detail.

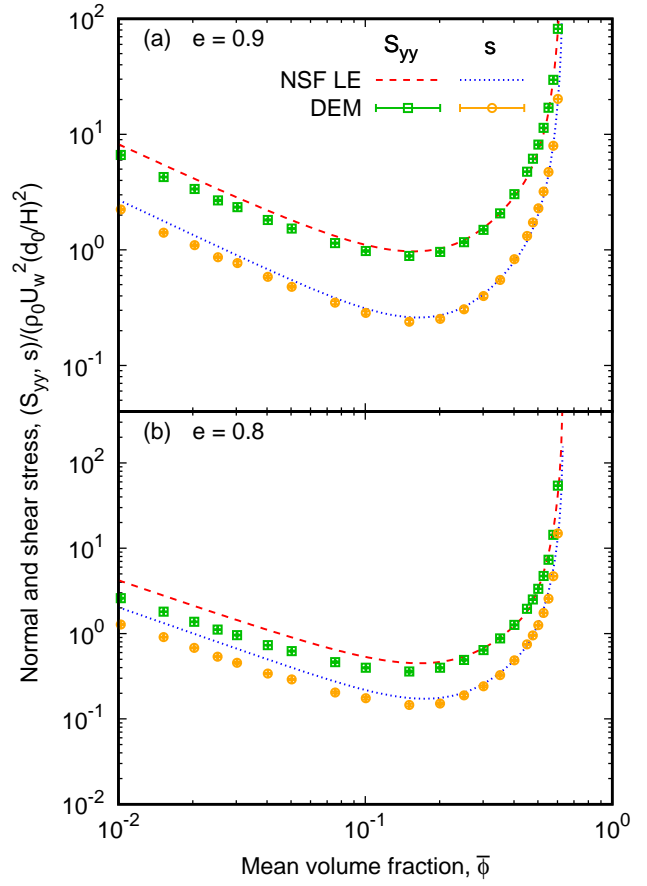


Figure B2: Variation in the normal and shear stresses, S_{yy} and s , respectively, for simulations run under LE boundary conditions, for coefficients of restitution: (a) $e = 0.9$ and (b) $e = 0.8$.

References

- [1] S. J. Friedmann, N. Taberlet, and W. Losert, *Int. J. Earth Sci.* **95**, 911 (2006).
- [2] S. Cuomo, *Geoenvironmental Disasters* **7**, 1 (2020).
- [3] B. Soundararajan, D. Sofia, D. Barletta, and M. Polletto, *Addit. Manuf.* **47**, 102336 (2021).
- [4] S. Haeri, Y. Wang, O. Ghita, and J. Sun, *Powder Technol.* **306**, 45 (2017).
- [5] S. Haeri, *Powder Technol.* **321**, 94 (2017).
- [6] V. Ganesan, K. Rosentrater, and K. Muthukumarapan, *Biosyst. Eng.* **101**, 425 (2008).
- [7] F. Jian, R. B. Narendran, and D. S. Jayas, *J. Stored Prod. Res.* **81**, 11 (2019).
- [8] C. E. Brennen, “Granular Flows,” in *Fundamentals of Multiphase Flow* (Cambridge University Press, 2005) pp. 252–271.
- [9] Y. Forterre and O. Pouliquen, *Annu. Rev. Fluid Mech.* **40**, 1 (2008).
- [10] P. R. Rao, K. K. and Nott, *An Introduction to Granular Flow* (Cambridge University Press, New York, 2008).
- [11] F. da Cruz, F. Chevoir, J.-N. Roux, and I. Iordanoff, in *Transient Processes in Tribology*, Tribology Series, Vol. 43, edited by G. Dalmaz, A. Lubrecht, D. Dowson, and M. Priest (Elsevier, 2003) pp. 53–61.
- [12] N. Sela and I. Goldhirsch, *J. Fluid Mech.* **361**, 41 (1998).
- [13] V. Garzó and J. W. Dufty, *Phys. Rev. E* **59**, 5895 (1999).
- [14] A. Santos, *Phys. A (Amsterdam, Neth.)* **321**, 442 (2003).
- [15] P. R. Nott, *J. Fluid Mech.* **678**, 179 (2011).
- [16] C. K. K. Lun, S. B. Savage, D. J. Jeffrey, and N. Chepurnyy, *J. Fluid Mech.* **140**, 223 (1984).
- [17] S. Abu-Zaid and G. Ahmadi, *ASCE J. Eng. Mech. Div.* **116**, 379 (1990).
- [18] C. K. K. Lun and S. B. Savage, *J. Appl. Mech.* **54**, 47 (1987).
- [19] S. Chialvo and S. Sundaresan, *Phys. Fluids* **25**, 070603 (2013).
- [20] D. Vescovi, D. Berzi, P. Richard, and N. Brodu, *Phys. Fluids* **26**, 053305 (2014).
- [21] C. S. Campbell and C. E. Brennen, *J. Fluid Mech.* **151**, 167 (1985).
- [22] M. W. Richman, *Acta Mech.* **75**, 227 (1988).
- [23] S. K. Dadzie, *J. Fluid Mech.* **716**, R6 (2013).
- [24] L. Wu, H. Liu, J. M. Reese, and Y. Zhang, *J. Fluid Mech.* **794**, 252 (2016).
- [25] S. K. Dadzie and C. Christou, *Int. Commun. Heat Mass Transfer* **78**, 175 (2016).
- [26] C. Christou and S. K. Dadzie, *J. Heat Transfer* **139** (2017), 10.1115/1.4036340, 092002.
- [27] C. Christou and S. K. Dadzie, *J. Phys. Commun.* **2**, 035002 (2018).
- [28] A. Stamatiou, S. K. Dadzie, and M. H. L. Reddy, *J. Phys. Commun.* **3**, 125012 (2019).
- [29] D. A. Lockerby and J. M. Reese, *J. Comp. Phys.* **188**, 333 (2003).
- [30] M. H. L. Reddy and M. Alam, *Phys. Rev. Fluids* **5**, 044302 (2020).
- [31] M. Knudsen, *Ann. Phys. (Berlin, Ger.)* **333**, 75 (1909).
- [32] S. K. Dadzie and H. Brenner, *Phys. Rev. E* **86**, 036318 (2012).
- [33] H. Brenner, *Int. J. Eng. Sci.* **54**, 67 (2012).
- [34] H. Brenner, *Phys. Rev. E* **86**, 016307 (2012).
- [35] L. M. H. Reddy and S. K. Dadzie, *Phys. Rev. E* **104**, 035111 (2021).

- [36] C. Kloss, C. Goniva, A. Hager, S. Amberger, and S. Pirker, *Prog. Comput. Fluid Dyn.* **12**, 140 (2012).
- [37] P. R. Nott, M. Alam, K. Agrawal, R. Jackson, and S. Sundaresan, *J. Fluid Mech.* **397**, 203 (1999).
- [38] M. Alam and P. R. Nott, *J. Fluid Mech.* **377**, 99 (1998).
- [39] M. Alam, V. H. Arakeri, P. R. Nott, J. D. Goddard, and H. J. Hermann, *J. Fluid Mech.* **523**, 277 (2005).
- [40] N. F. Carnahan and K. E. Starling, *J. Chem. Phys.* **51**, 635 (1969).
- [41] S. K. Dadzie, J. M. Reese, and C. R. McInnes, *Phys. A (Amsterdam, Neth.)* **387**, 6079 (2008).
- [42] D. Berzi, *Acta Mech.* **225**, 2191 (2014).
- [43] J. T. Jenkins and D. Berzi, *Granul. Matter* **14**, 79 (2012).
- [44] A. M. Tomy and S. K. Dadzie, *Micromachines* **13** (2022), 10.3390/mi13091425.
- [45] M. H. L. Reddy, S. K. Dadzie, R. Ocone, M. K. Borg, and J. M. Reese, *J. Phys. Commun.* **3**, 105009 (2019).
- [46] S. K. Dadzie and J. M. Reese, *Phys. Rev. E* **85**, 041202 (2012).
- [47] S. K. Dadzie and J. M. Reese, *Phys. Lett. A* **376**, 967 (2012).
- [48] N. G. Berloff, M. Brachet, and N. P. Proukakis, *Proc. Natl. Acad. Sci. U. S. A.* **111**, 4675 (2014).
- [49] M. H. L. Reddy and M. Alam, *J. Fluid Mech.* **779**, R2 (2015).
- [50] A. W. Lees and S. F. Edwards, *J. Phys. C: Solid State Phys.* **5**, 1921 (1972).
- [51] MATLAB, *MATLAB version 9.10.0 (R2021a)* (The Mathworks, Inc., Natick, Massachusetts, 2021).